Infrared photoinduced force near-field spectroscopy of silicon carbide

Kuan-Ting Wu, Youssef El-Helou, Elise Usureau, Enora Vuillermet, Michel Kazan, Mihai Lazar, Gaël Gautier, Wei-Yen Woon, Aurelien Bruyant

Infrared photoinduced force near-field spectroscopy of silicon carbide

Kuan-Ting WU[a,b,c], Youssef El-Helou[a,d], Elise Usureau[a], Enora Vuillermet[a], Michel Kazan[a,d], Mihai Lazar[a], Gaël Gautier[e], Wei-Yen Woon[b,c], Aurelien BRUYANT[a]

[a]*L2n, University of Technology of Troyes, CNRS UMR 7076, Troyes, 10004, France*
[b]*Department of Physics, National Central University, Taoyuan, 32001, Taiwan*
[c]*Molecular Science and Technology Program, Taiwan International Graduate Program, Institute of Atomic and Molecular Science, Academia Sinica, Taipei, 10617, Taiwan*
[d]*Department of Physics, American University of Beirut, Beirut, 11-0236, Lebanon*
[e]*GREMAN, INSA Centre Val de Loire, Université de Tours, CNRS UMR 7347, Tours, 37071, France*

Abstract

Silicon carbide (SiC) is a promising microelectronic semiconductor with an infrared response that depends on factors such as polytype, growth conditions, or structuring. Recent advances in infrared nano-imaging techniques provide new opportunities to characterize thin films at the nanoscale. We performed tip-enhanced near-field spectral characterization on various 4H-SiC sample surfaces using photoinduced force microscopy (PiFM). The near-field spectra feature a peak associated with a surface phonon polariton (SPhP) resonance, which proves to be highly sensitive to the material's surface quality. Interestingly, we found that the power absorption at the tip-sample junction, enhanced by the effective tip polarizability, can account for these PiFM spectra, resulting in a blend of both dispersive and dissipative spectral line shapes. As a potential application, a junction-field effect transistor is imaged to evaluate the technique's ability to map the surface of different p- and n-doped areas, demonstrating high sensitivity and spatial resolution compared to Raman analysis.

Keywords: Photoinduced Force Microscopy, Infrared nanoscopy, Silicon Carbide, Surface Phonon Polariton, Contamination layer

1. Introduction

Silicon carbide (SiC) has gained recognition for the development of high-power and high-frequency devices [1, 2], notably due to its wide bandgap. Its superior strength, thermal conductivity, chemical inertness make SiC a great material to operate in harsh environments such as nuclear reactors [3, 4]. Recent advancements in the manufacturing and structuring of SiC materials have significantly enhanced their performance, expanding their range of applications. This extended scope encompasses quantum photonic systems [5, 6], nano-systems [7, 8], including nano field emitters and nano field-effect transistors, as well as nano sensors, owing to SiC's biocompatibility [9, 10].

As various polytypes, doping, defects engineering, or structuring are employed in the development of this microelectronic material, there is a clear need for advanced non-destructive probing techniques to finely control and tailor SiC properties at the nanoscale. While desirable, achieving nanoscale lateral precision and probing depth resolution remains challenging with conventional characterization techniques, such as Raman [11] and Fourier-transform infrared (FTIR) spectroscopy [12], mainly due to the spatial diffraction limit. The advent of nano-infrared tools offers new opportunities to investigate material properties locally, including crystallinity, conductivity, and stress.

Over the last decades, several tip-enhanced near-field techniques have been developed, based on atomic force microscopy (AFM) combined with continuous or power-modulated laser directed toward the tip apex. These techniques enable localized spectroscopy and chemical imaging with spatial resolution at tip's scale through various signal extraction methods.[13–18]. Notably, infrared scattering-type scanning near-field optical microscopy (s-SNOM) has been effective in imaging SiC samples at the nanoscale [13, 19–24]. In this technique, the far-field scattered light from the tip-sample junction is typically modulated by the AFM tip working in tapping mode and subsequently demodulated at a carefully selected frequency using an interferometric detection scheme.

These s-SNOM studies demonstrate that slightly below the longitudinal phonon mode frequency, the material interface supports a surface phonon polariton (SPhP) mode that can be excited through tip-induced coupling. The intensity of this surface mode strongly depends on the imaginary part of the local material dielectric function. As a result, the near-field spectrum in this spectral region is a good indicator of the local crystal quality or doping, encouraging further investigation across a broader range of SiC samples with varying qualities, polytypes, doping levels, etc. On the other hand, the residual sensitivity of s-SNOM to the tip environment within the detection spot [25] advocates for exploring alternative scanning-probe techniques, either separately or in combination.

In comparison, photo-induced force microscopy (PiFM) exploits the laser-induced mechanical forces at the tip-sample junction. This approach, which detects forces mechanically similar to AFM, aims to provide an almost background-free signal [17, 18, 26], where the "background" refers to the unwanted

scattering contribution within the laser focus spot. To obtain the near-field PiFM spectrum, the photoinduced force sensed by the tip cantilever is recorded at different incident laser wavelengths, while the metal-coated tip is oscillating with a small set-point amplitude (e.g. 2 to 3 *nm*) modulated in the attractive van der Waals (vdW) force regime, commonly referred to as a non-contact AFM mode [27–32].

Previous PiFM reports have notably demonstrated the technique's capability to detect surface modes related to phonons [33], notably in 2D materials [34]. Several mechanisms have been identified as potentially contributing to the forces sensed by the cantilever. One mechanism involves the dipole-image dipole force between the oscillating dipoles of the tip and the sample surface, which depends on a complex effective polarizability and results in a more dispersive spectral lineshape [35–38]. In contrast, observations in polymers reveal more Lorentzian, "dissipative" spectral lineshapes that correlate well with the material absorption spectra determined through FTIR [28, 29, 39–41]. Dissipative mechanisms have been linked to periodic photothermal expansion leading to modulated van der Waals (vdW) forces [30, 42] and potentially photo-acoustic forces [37, 43]. Additionally, opto-mechanical damping [31] of the tip resonance caused by incident light at the tip-sample junction has also been highlighted.

In this work, we present the PiFM spectral investigation of SiC samples having received different treatments. We show that the near-field spectra within the material reststrahlen band (RB) is sensitive to the surface quality, especially near the SiC surface phonon-polariton (SPhP) frequency, below which a prominent PiFM peak is observed and could be used to estimate the sample quality. Using the experimentally determined dielectric function of a 4H-SiC substrate, we then propose a simple analytic model for the PiFM signal by evaluating the absorbed energy in the sample near the tip-sample junction, where both dispersive and dissipative effects are included via the effective polarizability and material absorption respectively. Finally, as a potential application, a junction-field effect transistor (JFET) is imaged to evaluate the sensitivity of the main PiFM peak to the different doped regions.

2. Experiment

The PiFM investigation was performed using a VistaScope system from Molecular Vista, Inc. using contamination-free gold-coated silicon cantilevers (NCHAu). The system operates in non-contact mode, with side illumination coming from a tunable mid-infrared quantum cascade laser (QCL) focused at the tip apex with a high-numerical aperture parabolic mirror, within the spectral tunability range 770-1860 cm^{-1}. A schematic is shown in Figure 1, highlighting the 1st and 2nd mechanical resonance of the cantilever, noted f_0 (∼250 kHz) and f_1 (∼1.6 MHz). These two resonances are used to simultaneously acquire the photoinduced force (PiF) and the AFM topography of the sample. By default, the PiF signal is detected at f_0, while the cantilever is driven at f_1 for the non-contact AFM topography feedback.

The incident light is power-modulated at the frequency f_m which can take two different values corresponding to two distinct modes. In the so-called "Direct mode", the overall photoinduced forces are induced by driving the laser intensity at the low-frequency mechanical resonance, i.e $f_m = f_0$. In the "Sideband mode", which is the preferred mode, an optical heterodyne method [44, 45] is used, where the laser modulation is $f_m = f_1 - f_0$. In that case, it is typically considered that the gradient (derivative) of the photo-induced force along the z direction is probed so that the light scattering force is removed, resulting in an almost background free signal [18, 26]. Recording the PiFM signal with the laser scanning through the laser spectral range, PiFM spectra were obtained. To investigate how surface properties such as implantation, doping, and porosity influence the PiFM spectra, point spectral measurements were performed on several 4H-SiC substrates, which are listed and briefly described in Table 1.

Table 1: 4H-SiC Sample Descriptions

No.	Doping	Description
1	N	Bulk
2	N	Al-ion implanted (RT) area
3	N^+	contains 20% porosity area
4	N	∼150 *nm* thick amorphous, annealed at 1700 °C
5	N	∼150 *nm* thick amorphous, annealed at 1400 °C

The first 4H-SiC sample was purchased from Cree Inc. The substrate is N-doped, with a free carrier concentration of $10^{18}\,cm^{-3}$ at room temperature, with an on-axis (c-axis oriented) surface. The second sample is another commercial N-doped substrate with a 4° off-axis surface, partially treated with an Al-ion implantation with a dose of $1.75 * 10^{15}\,cm^{-2}$. Sample 3 is an N^+-doped substrate containing a localized porous area with 20% porosity, achieved through anodization in an HF-based solution [46]. On another commercial N-doped (off-axis) 4H-SiC substrate, a ∼150 *nm* thick amorphous SiC layer was deposited on the surface by electron-beam evaporation technique with an Elettrorava machine. The sample was then cut into two pieces and annealed for 30 minutes in an rapid thermal processing furnace (RTP, AET Technologies) at 1700 °C (Sample 4) and 1400 °C (Sample 5), respectively, while typical SiC epitaxial films are grown at 1500-1650°C by chemical vapor deposition [47]. To prevent the formation of a graphitic layer on the SiC surface, graphite capping was employed [48]. Further detail can be found in these references.

As an initial point of comparison, we conducted far-field infrared reflectivity measurements on sample 1, using a homemade FTIR in the range of $700 - 4000\,cm^{-1}$. The far-field spectral analysis was also used to determine the complex anisotropic dielectric function ($\epsilon = \epsilon' + i\epsilon''$) of the bulk material as detailed in [49]. Advantageously, the knowledge of this bulk material response provides the main longitudinal (LO) and transverse (TO) optical phonon frequencies delimiting the RB ($800 - 988\,cm^{-1}$), and serves as initial input to feed a model accounting for the PiFM response, as will be detailed in the results part.

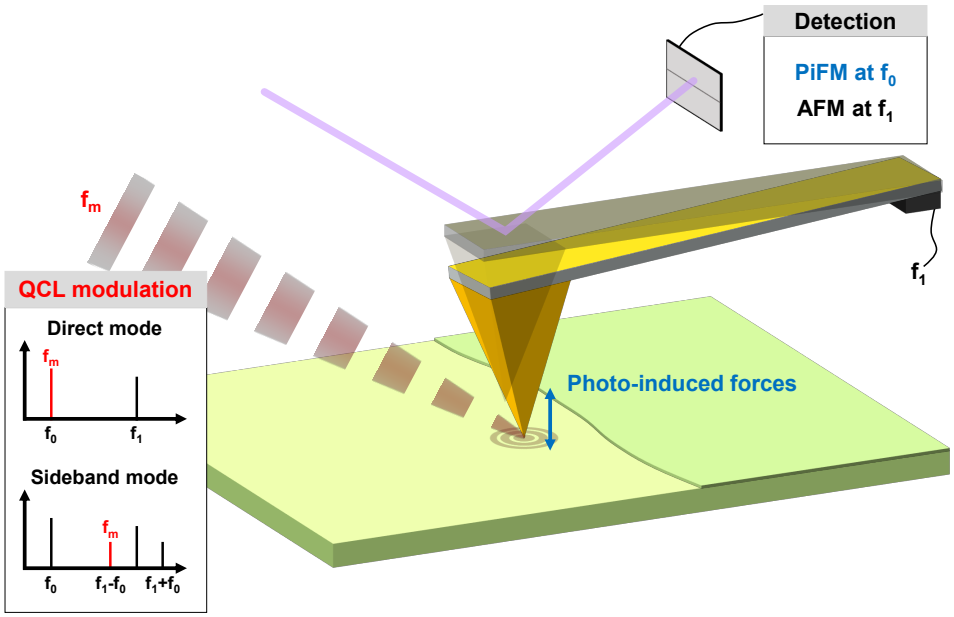

Figure 1: Schematic diagram of the PiFM system and detection modes. The photo-induced force is recorded by measuring the amplitude of the first mechanical resonance at frequency f_0 while the AFM is working in non-contact mode at the second frequency f_1. A pulsed tunable IR laser with an adjustable repetition rate f_m is focused at the tip-sample junction with either $f_m = f_0$ (direct mode) or $f_m = f_1 \pm f_0$ (sideband mode).

3. Results

3.1. PiF spectra obtained on 4H-SiC samples

In Figure 2(a), typical PiF spectra of the 4H-SiC (Sample 1) are presented, in both direct and sideband detection modes. In both cases, two main peaks are observed, one around the TO frequency near 805 cm^{-1}, and another around 920 cm^{-1}, below the LO frequency. In sideband mode, the signal predominantly falls within the RB of the SiC, where the real permittivity ϵ' of the sample is negative and the loss term ϵ'' is significant. A strong minimum is observed in the 950-1030 cm^{-1} range, followed by a broad bump around 1030-1300 cm^{-1}, shortly discussed later on. On the other hand, in direct mode, the near-field spectrum outside the RB of SiC exhibits a relatively flat PiF response.

As reported by [26], the sideband mode provides higher spectral contrast than the direct mode and provide higher spatial resolution. The scattering forces from the incident light, that contains more information from the bulk, are effectively removed, probing merely the response from the top most surface corresponding to the highest spatial frequencies of tip-enhanced field. In the following, only sideband PiF spectra were recorded. In order to compare the spectral shapes, the intensity of the PiF spectra on SiC samples are normalized to the mean intensity in the flat region of the sideband PiF spectra (at higher wavenumber).

The prominent PiF peak centered at 920 cm^{-1} is a signature of the crystalline SiC material, which is also observed in s-SNOM spectra on 4H-SiC [19, 20, 23]. Herein, this peak is named “red-shifted resonant peak" and is noted RRP on the figure. This RRP is related to the existence of a SPhP resonance near $\epsilon \approx -1$ but is red-shifted compared to it due to the coupling with the high tip polarizability. In s-SNOM, the RRP is explained by considering the scattering coming from the tip apex and its image through the sample, which is enhanced in the SPhP vicinity. In PiFM as well, a force related to the dipole-image dipole interaction near the SPhP resonance can be expected due to the stronger coupling of the oscillating charges in the tip with the optical phonons in the polar lattice.

In both cases, the laser focused at the tip-sample junction induces an oscillating dipole in the gold coated tip apex, and a mirror dipole on the sample side. The field being strongly confined at the tip apex in the sample’s near-field, the magnitude of the image dipole follows the quasi-static reflection coefficient $\beta = \frac{\epsilon-1}{\epsilon+1}$. In principle, the SPhP resonance is maximal when the complex dielectric function is close to the real value -1, below the LO frequency. However, while β is maximal in that case, the tip-sample coupling tends to substantially red-shift the overall resonance of the probe-sample system. In the PiFM measurement, where tip sample distance is small, a relatively large red shift of about 40 cm^{-1} is observed between the RRP and the frequency where $\epsilon' = -1$, as can be seen in Figure 2. In fact, the spectral position of the signal maxima is better described using the tip dipole’s effective polarizability α_{eff} which is function of the bare dipole tip polarizability, β and tip-sample distance. This effective polarizability which accounts for driving field correction within the tip caused by the image dipole was primarily used in s-SNOM modeling to express the detected far-field back-scattering [19, 23, 36, 50–52]; its expression is recalled in the modeling section.

The circled shoulder peak near 850 cm^{-1} and the bump centered near 1100 cm^{-1} showed little consistency from tip to tip, typically exhibiting an increase with the usage of the tip. These spectral features stem from compounds of silicon oxides and

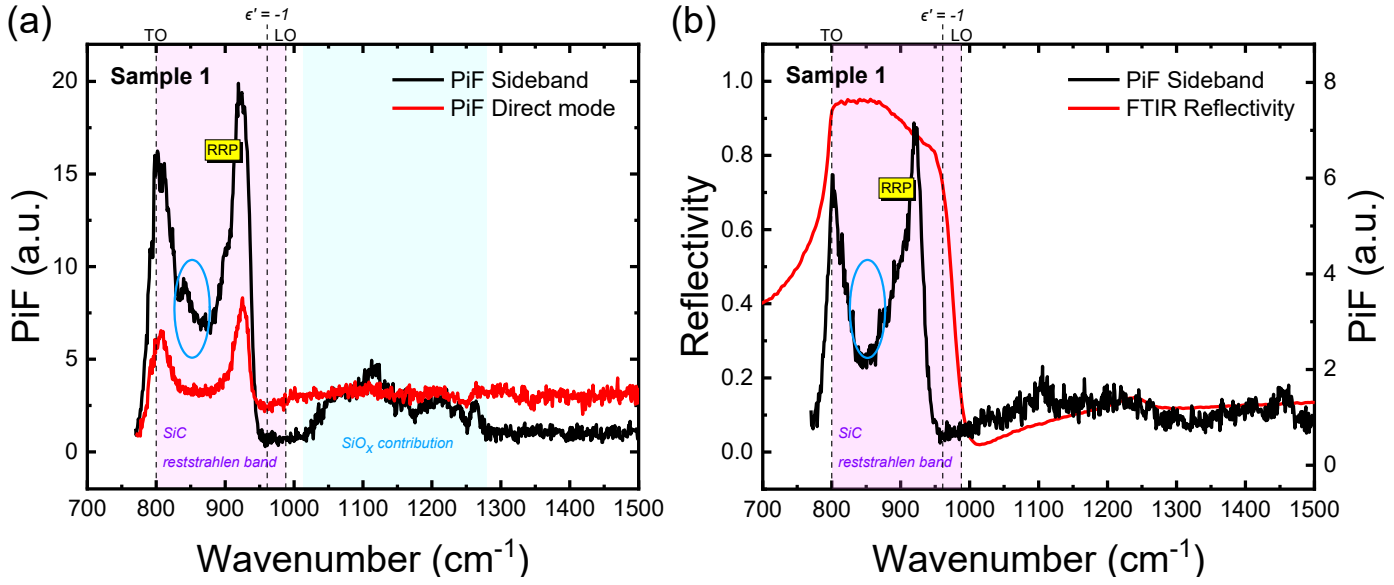

Figure 2: (a) PiF spectra on bulk 4H-SiC (Sample 1), using sideband (black) and direct (red) detection modes. RRP stands for "red-shifted resonant peak." The (blue) circled shoulder peak near 850 cm^{-1} showed little consistency from tip to tip. (b) Another sideband PiF spectra on Sample 1 taken with a new tip (less contamination) is plotted in black. In comparison, FTIR reflectivity spectrum on Sample 1 is shown in red.

hydrides [53, 54], denoting the degradation of the tip coating, or the presence of the contaminating nano particles, water layer and other compounds from the environment, which are generally difficult to avoid in AFM-based systems (Cf. supplemental information in [30] and [55, 56] for example). Figure 2(b) shows another sideband PiF spectrum also taken on Sample 1 with a brand new tip, where the mentioned features (side-peak at ~850 cm^{-1} and bump) are reduced. Similar trends were observed in other samples, indicating that we should focus our attention on the other spectral features that are directly related to SiC, primarily within the RB. To ensure that the PiF spectra are comparable, each set of spectra was obtained using the same tip within a short period.

Compared to the measured PiF spectrum, the provided FTIR spectrum shows a reflection plateau in the RB mostly covering the 800-988 cm^{-1} range. The low frequency rising edge is close to the TO phonon mode (800 cm^{-1}), while the minimum of the valley is close to the LO phonon mode (988 cm^{-1}) [57]. PiF spectra have been shown previously to match well with the FTIR absorption spectrum (mostly on polymers) [28, 29, 39–41, 58] indicating that the material's optical loss is a key parameter to account for the near-field spectrum. Remarkably, in the case of crystal with strong optical phonon such as SiC, the absorption (1-R) differs strongly from the near-field signal and the local field enhancement cannot be ignored.

Figure 3(a) shows the sideband PiF spectra obtained on the implanted 4H-SiC substrate, i.e Sample 2. In contrast to the non-implanted area, the SPhP-related RRP disappears in the implanted area. Similar trends were found on the N^+-doped porous 4H-SiC, Sample 3. The resonant peak appears only on the area without porosity (Fig. 3(b)). Notably, the RRP intensity on the N^+-doped Sample 3 substrate is weaker compared to the N-doped Sample 1.

On the amorphous SiC thin (~150 *nm*) film evaporated on a 4H-SiC substrate (Sample 4,5) as well, the reduced RRP in the spectrum indicates the poor surface crystalline quality Fig. 4. After high temperature annealing, a strong red-shifted resonant mode is re-obtained. Compared to the 4H-SiC supporting substrate, this SPhP-related mode is stronger on the 1700 °C annealed SiC thin film. On the 1400 °C annealed thin film, the RRP is recovered to a similar intensity but with a larger red shift. Such reinforcement can be attributed to a SiC thin film re-crystallization [59]. In the Raman spectra of Sample 4 and Sample 5, as shown in [47], the LO-related phonon peaks reappear following high-temperature annealing. However, it is important to note that the variation in Raman peak intensities across different annealing temperatures is relatively minor in these thin films. Overall, lower contrast was observed in the Raman analysis of heterogeneous samples, as illustrated later in Section 5.

In Figure 5, we show the topography and sideband-PiF images simultaneously obtained at the smooth boundary between the evaporated SiC thin layer and the 4H-SiC substrate (for Sample 4 and Sample 5, after annealing).

In the topography images Fig. 5(a,b), the higher areas indicate the deposited SiC thin film region, while the lower areas correspond to the 4H-SiC substrate. With the excitation laser at 921 cm^{-1}, the PiF images Fig. 5(c,d) show opposite contrast between the thin film and the substrate for each sample. Figures 5(e,f) display the corresponding cross-sectional profiles of the topography and PiF images. Notably, when the thin film on Sample 4 (annealed at 1700 °C) is approximately 40 *nm* thick, the measured PiF signal is lower than that on the substrate. In contrast, Sample 5 (annealed at 1400 °C) shows a sharp increase in the PiF signal as the thin film thickness decreases. Overall, our experiments indicate that the SPhP mode detected by PiFM

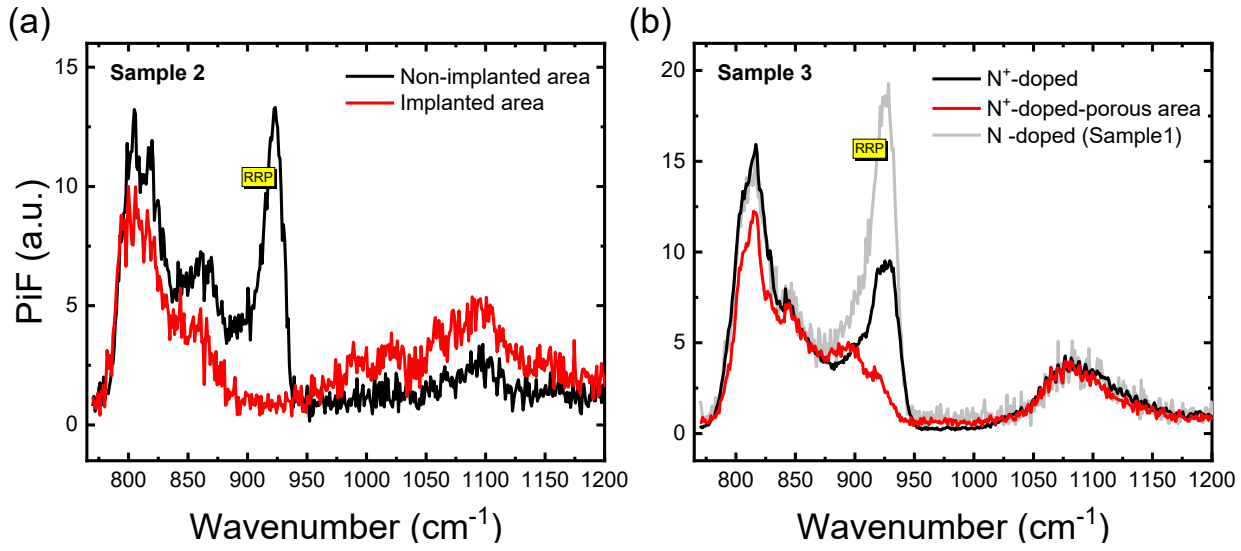

Figure 3: Near-field spectra showing the quality-dependent intensity of the RRP, performed on (a) non-implanted (black) and implanted (red) surfaces on a bulk 4H-SiC (Sample 2); (b) non-porous (black) and porous (red) areas on an N^+-doped 4H-SiC substrate (Sample 3). Spectrum of an N-doped Sample 1 (grey) was also taken to compare.

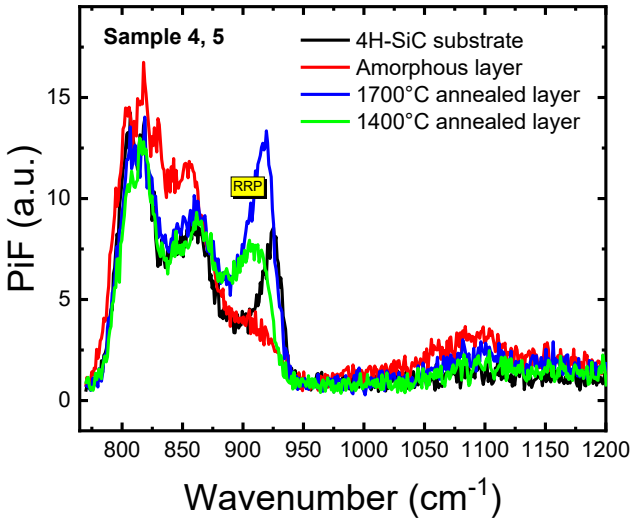

Figure 4: Sideband PiF spectra made on a bulk 4H-SiC substrate (black), the ~150 *nm* thick amorphous SiC layer evaporated on it (red), and the afterward separated samples (Sample 4,5) annealed at 1700 °C (blue) and 1400 °C (green).

on 4H-SiC is highly sensitive to surface quality and can serve as an effective indicator for nanostructure imaging. Further interpretations of these findings are provided through the model presented hereafter.

3.2. *PiF model based on effective polarizability enhanced absorption*

Previous studies on PiFM revealed that both induced dipole-dipole force and near-field thermal effects can contribute to the observed spectroscopic contrast, depending on the material properties of the sample [37, 40]. Recently, [38, 40] showed that the induced dipole force is more intense on materials with strong oscillator, which exhibit greater polarizability with a negative real part of the dielectric function ϵ', particularly near $\epsilon' = -1$, where the resonance of surface plasmon polaritons (SPPs) or SPhPs occurs. On the other hand, the magnitude of the induced thermal forces is directly influenced by the photo-absorption near the material surface. An interesting and relatively simple analytical model has been proposed based on the evaluation of an effective absorption coefficient [30], which assumes relatively low absorption regime and subwavelength samples [60]. However, this approximation seems relatively out of range in the RB region of polar crystal where the absorption is strong, and this model could not capture the observed RRP in our measurements.

To predict the dipole-dipole force and the photothermal response, the knowledge of material's dielectric function $\epsilon(\omega)$ is needed. For the bulk 4H-SiC, this function is well described by the a damped Lorentz oscillator model with addition of Drude's term for the free carrier contribution [13]:

$$\epsilon(\omega) = \epsilon_\infty + \Sigma_{j=1}^{3} \frac{S_j \omega_{TO,j}^2}{\omega_{TO,j}^2 - \omega^2 - i\Gamma\omega} + \chi_{Drude} \qquad (1)$$

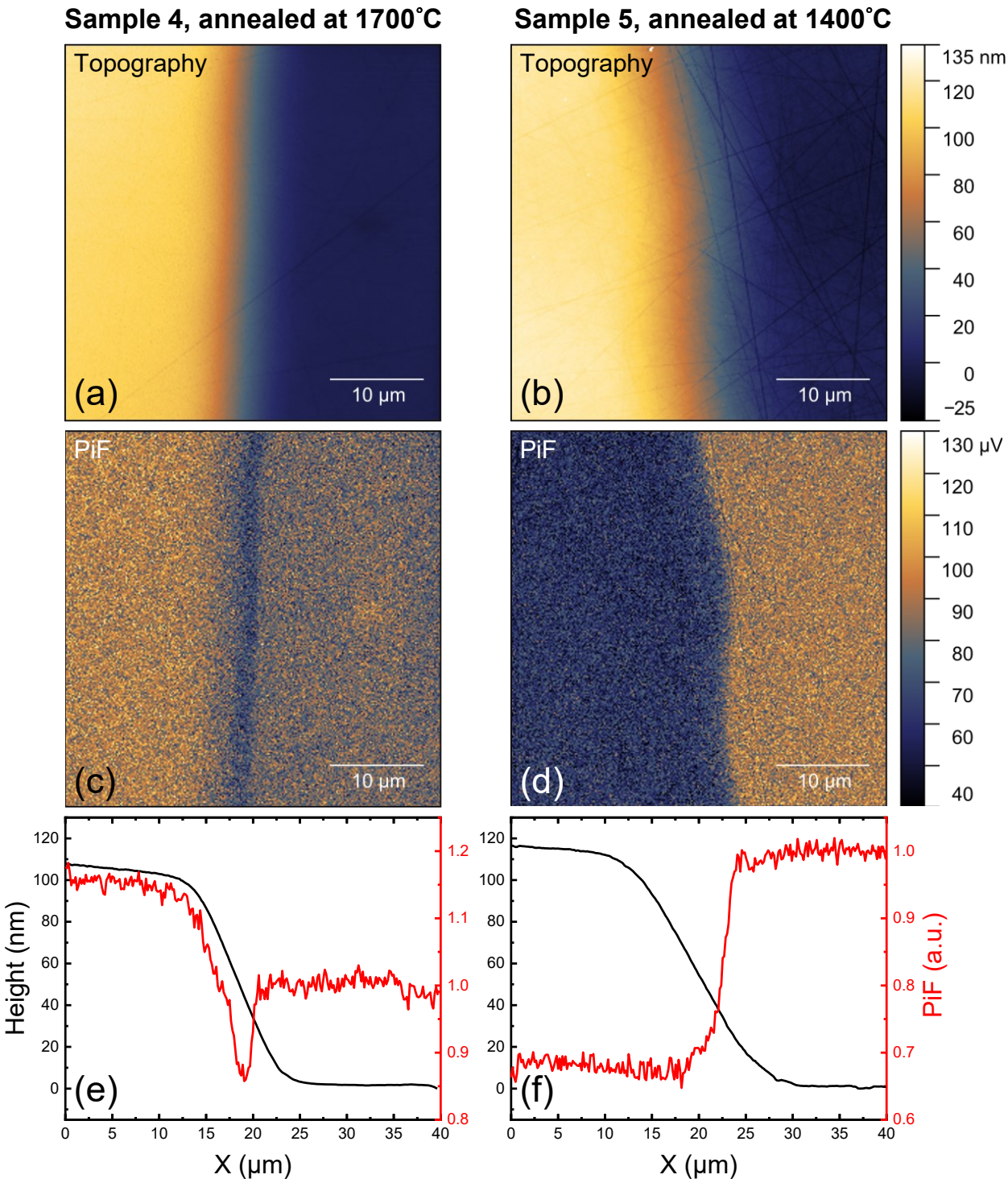

Figure 5: Topography and sideband PiF images, with excitation laser at the SPhP mode (921 cm^{-1}), obtained simultaneously at the boundaries between the evaporated SiC layer and the 4H-SiC substrate after annealing at (a, c) 1700 °C, and (b, d) 1400 °C, respectively. (e, f) show the corresponding cross-section profiles. For better comparison, the PiF intensity in red was normalized by the mean value obtained on the substrate area of each sample.

The parameters were determined on the reference Sample 1 by fitting the reflectivity FTIR measurement [49]. Along the c-axis, considered as the direction probed by the tip, besides the already given LO and TO phonon frequencies, the high frequency permittivity $\epsilon_\infty = 5.53$, the phonon oscillator strength $S = 2.86$ and damping $\Gamma = 2\,cm^{-1}$ were determined, as well as the parameters of the Drude's susceptibility given by:

$$\chi_{Drude} = -\frac{1}{\tilde{\omega}^2 + \frac{\tilde{\omega}}{\tilde{\tau}}i}, \tag{2}$$

with $\tilde{\omega} = \frac{\omega}{\omega_p}$ and $\tilde{\tau} = \tau \cdot \omega_p$, consisting in the plasma frequency $\omega_p = 1450\,cm^{-1}$ and the dimensionless relaxation time $\tilde{\tau} = 0.3915$.

Also these parameters coming from far-field measurement were used as inputs to fit the obtained PiFM near-field spectra, except for the phonon damping rate, which needed to be increased to $\Gamma = 17\,cm^{-1}$. This increased value is presumably attributed to surface defects and contamination, becoming more influential in the tip-enhanced near-field setup, although surface damping related to other mechanisms could play a role. [20, 23, 61, 62]

Figure 6(a) plots the experimentally determined dielectric functions of Sample 1, initially used for near-field simulation. These curves provide the extinction coefficient $\kappa = Im(\sqrt{\epsilon})$ given on Figure 6(b). By comparing the PiFM near-field spectra and the loss term ϵ'' or the extinction coefficient, we see that although the TO peak on the low-frequency hand has some resemblance with the loss term, the photoexpansion induced by the absorption of the illuminating laser can hardly explain the two observed PiFM peaks. In fact, the far-field illuminating the sample is mostly reflected by the sample within the RB, especially for a relatively large angle of incidence. On the other hand, the evanescent nano-source confined at the scattering tip is enhanced by the elongated probe shape and can be efficiently absorbed by the sample. To determine the tip enhanced absorption at the sample surface, we need to consider both the loss term and a frequency-dependent enhancement from the sharp tip and its image induced through the sample.

Generally, the total optical absorption power in a given volume is $P = \int Q(r)dV$, with the absorption power density $Q(r)$ in (W/m^3) given by the divergence of the time-averaged Poynting's vector. In our case of a PiFM tip detecting only the forces along the z axis in the tip-sample junction, it can be written as $P = A \int Q(z)dz$, with A a small cross-sectional area below the tip apex. Determining the absorbed power then requires to determine the local field $\mathcal{E}(z)$ within the absorbing medium since $Q(z)$ is given by:

$$Q(z) = \frac{1}{2}\omega|\mathcal{E}(z)|^2\epsilon_0\epsilon'' \tag{3}$$

where $\mathcal{E}(z)$ is the evanescent electric field below the surface ($z < 0$) which is generated by the tip . As in s-SNOM, we need to consider that the tip is both illuminated directly and through a reflection, where the incident light is mostly p-polarized, therefore:

$$Q(z) \propto \frac{1}{2}\omega|1 + r_p||\alpha_{eff}\,E(z)|^2\epsilon_0\epsilon'' \tag{4}$$

with r_p the sample reflectivity derived from Fresnel equations, ϵ_0 the vacuum permittivity and where the loss term resumes to the imaginary part of the plotted complex dielectric function of the sample, considering only the component aligning with the c-axis of SiC, i.e. along the tip axis. In this formula, the field magnitude scales with the effective induced dipole proportional to $|1 + r_p||\alpha_{eff}|$ that accounts for the enhanced field at the tip apex considering the self-field generated by the probe image. Finally, the z dependence within the sample is given by:

$$E(z) = \tau\,E(0^-)e^{-Im(k_z)z}, \tag{5}$$

where τ is the transmission coefficient of the considered evanescent waves that can be evaluated in the quasi-static limit though $\tau = \frac{2\sqrt{\epsilon}}{\epsilon+1}$. The strong vertical confinement is accounted for by the imaginary part of $k_z = \sqrt{k^2 - k_{//}^2}$, the wave-vector associated with the considered evanescent wave along the z direction, where k is the wave-vector magnitude $\sqrt{\epsilon}\,2\pi/\lambda$ at the considered wavelength λ. For simplicity, a single characteristic spatial frequency $f = 1/a$ was used to evaluate the parallel component $k_{//} = 2\pi f$, a being the considered tip extremity diameter.

As detailed elsewhere in the context of s-SNOM [13, 23, 50–52], the effective polarizability of the tip and sample can be described with the point dipole model (PD) or the finite dipole model (FD). The point dipole model [50] regards the tip as a small polarizable sphere interacting with its image through the sample. In this model, the effective polarizability of the tip under the action of the incident external field, regarded as mostly polarized along the tip axis, is given by:

$$\alpha_{eff}^{PD} = \frac{\alpha_t}{1 - \frac{\alpha_t\beta}{16\pi(R+H)^3}}, \tag{6}$$

where α_t is the bare tip polarizability, β is the prior mentioned quasi-static reflection coefficient, defining the sample surface response. R is the radius of the sphere (tip apex) and $H(> R)$ is the tip height from the sample surface. The tip polarizability α_t being enhanced compared to the case of simple sphere(α), it is phenomenologically accounted for by multiplying the polarizability of a small spherical probe by "c" a complex valued constant: $\alpha_t = c * \alpha$, with typically $|c| > 1$ and $\alpha = 4\pi R^3(\epsilon_t - 1)/(\epsilon_t + 2)$. ϵ_t is the dielectric function of the sphere.

On the other hand, the finite dipole model [23, 52] simulates the tip as a long conductive spheroid of length $2L$. Due to the large separation of opposite charges in this elongated shape, the monopole charge at the tip apex interacts with the sample, leading to an effective polarizability written as [51]:

$$\alpha_{eff}^{FD} \propto 2L\left(1 + \frac{f_0\beta}{1 - f\beta}\right) \tag{7}$$

where f_0 and f are functions of the geometric parameters R/2L, H/2L as well as a factor g related to the amount of charge induced in the tip due to the self-field appearing in the presence of the surface. The detailed expressions and values are given in the appendix Appendix A.1.

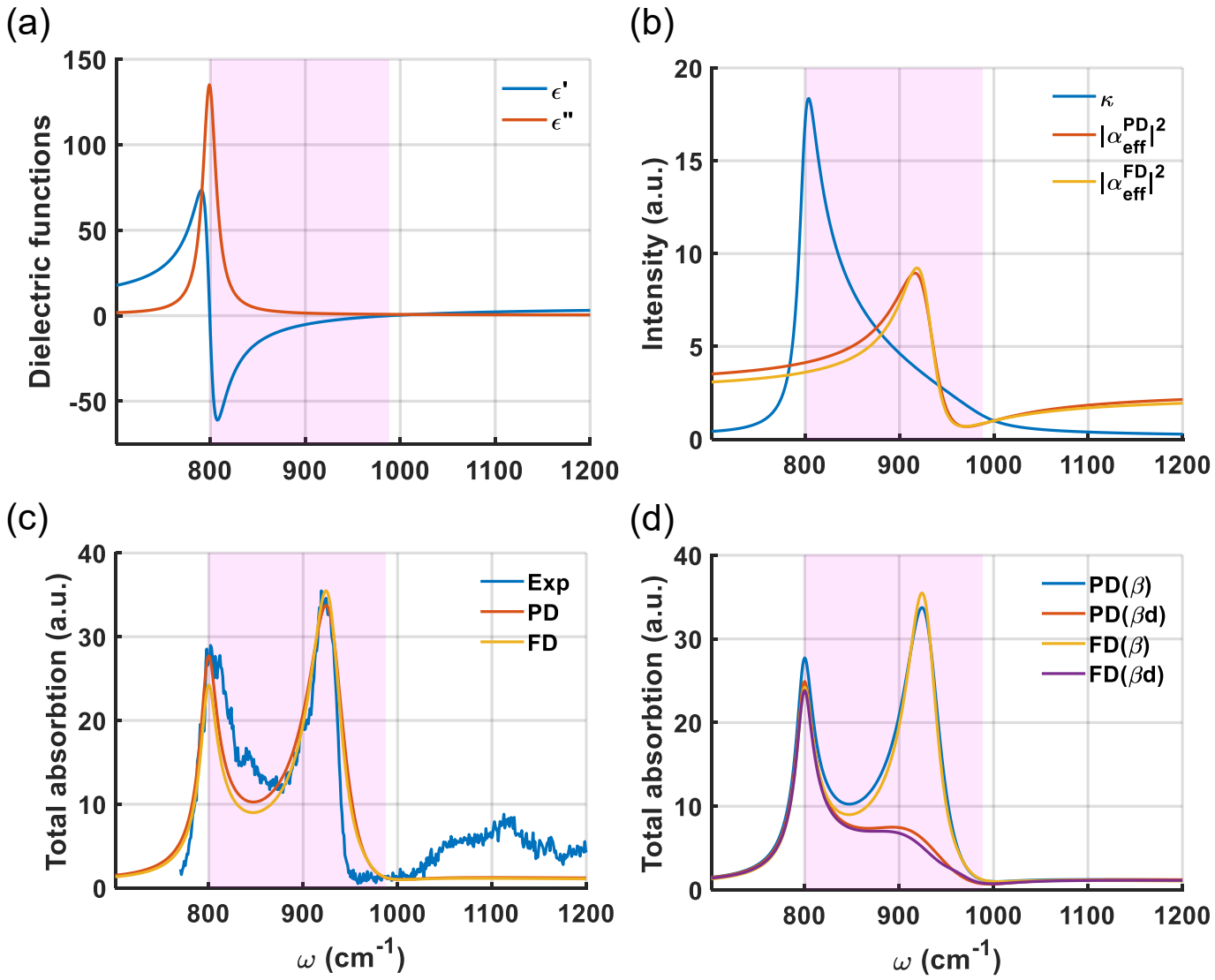

Figure 6: (a) Dielectric functions of Sample 1 derived from the FTIR spectrum. (b) The extinction coefficient of the sample is plotted in blue. Simulated effective polarizability with PD and FD models of the tip-sample junction is shown in red and orange, respectively. (c) Calculated total absorption at the tip-sample junction by the PD and FD model, comparing to the PiF spectrum showed in Figure 2(a). (d) Simulation results with the original β and the damped β.

Figure 6(c) plots the simulated total absorption (P) results, in comparison to the experimental data, normalized to the value at 1000 cm^{-1}. With $R = 25\,nm$, $H = 7\,nm$, $L = 400\,nm$, the finite dipole model fits qualitatively well the acquired spectra. With less parameters though, the point dipole model provides a similar fit quality using the complex factor $c = 3.8e^{0.14i}$. Finally, we see that the PiF spectra of the other SiC samples can be simulated by altering β, as showed in Figure 6(d). More details are given in the following discussion.

4. Discussion

Impact of SiC surface properties on the PiF response

Figures 3 and 4 show very substantial decreases in the RRP intensity across different SiC sample qualities, while the TO-related peak is much more stable. Some reduction of the RRP can be be accounted for by the presented model by increasing the sample loss term ϵ'' in the sample's dielectric function. A natural approach is to consider variations in the different quantities appearing in the dielectric function of the sample which can be related to implantation, higher doping or porosity. A parametric study is conducted in the appendix Appendix A.2 where reduction of the phonon and electron lifetimes, as well as possible increase in the carrier concentration are considered [20, 63, 64]. Figure A.11(c,f) shows that the simulated RRP shifts slightly with varying parameters, which may be connected to the observations made on the re-crystallized Samples 4 and 5 (Fig. 4). However, achieving sufficient RRP damping would require unrealistic modifications to the dielectric function, which would alter the observed spectra beyond the RRP region. For example, a large increase in plasma frequency leads to greater absorption beyond the RB region. This high sensitiv-

ity to the material surface is likely due to a damping mechanism that effectively quenches field enhancement in the tip-sample gap, which is maximal in this spectral range.

An expression for this damping is not available within the current tip-sample interaction model, which relies solely on the simple point-dipole or finite dipole model used in Eq. 4. These models do not account for the actual shape of the probe, which necessarily influences field enhancement in the tip-sample gap, making it more sensitive to sample losses. Alternatively, one can hypothesize the need for additional damping terms, potentially arising from large lattice cracks, holes, or vacancies that might create spatial inhomogeneities in the sample's dielectric function. These extra damping effects can be phenomenologically embedded in the point or finite dipole model. In the point dipole model for example, the self-induced field in the probe resulting from the tip-sample interaction is obtained through the approximated Green's dyadic appearing in the effective polarizability denominator (cf. eq.6) as a term proportional to $\beta/(R+H)^3$. This term which multiplies the probe polarizability accounts for the probe-sample interaction and can be enhanced or damped via a complex factor d multiplied to the sample response β. Figure 6(d) presents the simulation results of a SiC sample of reduced surface quality with $d = 1.5e^{0.45i}$. The RRP is effectively quenched while the rest of the spectrum remains almost the same, reproducing qualitatively the observation on Samples 2-5.

Thickness dependence of the PiF signal on the annealed SiC thin films

Figure 5 showed the spatial dependence of the SPhP-related RRP across the boundary between evaporated SiC and non evaporated region, for the two annealed samples. By combining those AFM and PiF data, Figure 7 plots the PiF–thickness relation of both samples. Interestingly, the PiF signal remains similar to that of the substrate only below the first $25-30\,nm$. For the lower annealing temperature (Sample 5) in red, a quick signal decrease with the thickness due to the peak shift is observed. In contrast, PiF response for the higher annealing temperature (Sample 4) in black shows a limited intensity drop, followed by a rather linear increase as the layer is getting thicker. The non-monotonous transition is not yet fully explained and could involve dopants diffusion from the substrate. On the other hand, the supposedly polycristaline nature of the annealed layer can lead to a better excitation of the RPP mode for the thicker region. Further study considering a multilayer effect due to the structure heterogeneity (β) [40, 65] could also be considered with the help of hyperspectral PiFM images to better describe the observed transition.

Nature of the sensed PiFM force

We have seen that the PiF spectra on SiC can be simulated by the total absorption at the tip-sample junction, considering a field enhancement provided by the dipole models. As absorption of the modulated light induces periodic photoexpansion, this surface displacement entails a modulation of the non-contact vdW forces which is typically considered as inducing a

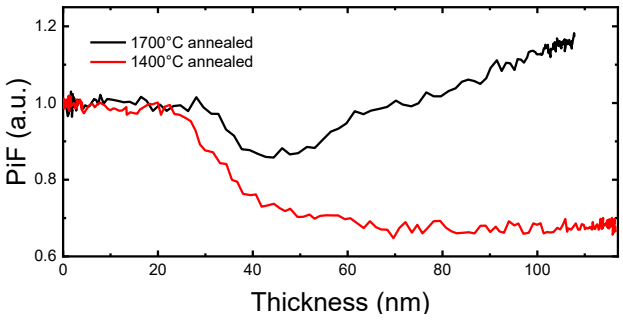

Figure 7: PiF intensity as a function of the SiC thin film thickness, at the initial RPP peak position ($921\,cm^{-1}$). The profiles were obtained from Figure 5 (e, f)

globally attractive force [30]. On the other hand, a pure optical dipole-dipole force is mostly considered as attractive as well [38, 40], also scaling with the effective polarizability α_{eff}, as in the model used in [36] in the case of a highly doped semiconductor (without phonon resonance). While the presence of a non negligible optical force cannot experimentally be ruled out, this force cannot explain the TO-related peak which requires the inclusion of the loss term in the signal expression. However other forces may be involved such as the optical scattering force as well as a photoacoustic force [37, 43] which would be intuitively regarded as a repulsive force. Therefore, more experimental insight on the force origin can be given by investigating the frequency responses of the first mechanical (PiF detection) mode (f_0) of the cantilever. Notably, forces acting on the oscillating AFM tip shift the resonance frequency of the tip cantilever: repulsive forces shift the resonance to a higher frequency, while attractive one lower the resonant frequency (Cf.[28–32]).

Figure 8(a) plots the resonant frequencies (black) and the intensities (red) of the first mechanical mode (f_0) of the cantilever while the tip-sample distance is stabilized through f_1. These two quantities were recorded on Sample 1 for selected optical wavenumbers across the PiF spectrum, operating in direct mode to facilitate the analysis. The natural frequency of the free oscillating cantilever is indicated by the black dotted line in the top area of the figure. The actual resonant frequencies during the measure remains at lower values, reflecting the fact that we operate the PiFM in the attractive vdW forces range only, as stated by previous studies. The lower black dashed line also indicates the resonant frequency when the tip is engaged on the SiC sample but without an incident laser.

When doing PiF, i.e. with the laser on, a global offset toward higher frequency is observed across the spectrum, which can be interpreted as an additional photo-induced repulsive force partially counteracting the stronger vdW forces. This upper shift could result from the near-field scattering forces or photoacoustic effect. However, at the incident laser of ~805 cm^{-1} and ~920 cm^{-1} corresponding to the PiFM maxima, less shift is comparatively detected, confirming that the two main peaks obtained on SiC samples are attractive PiF.

Another approach to determine the nature of the photo-induced force is the tip-sample distance dependence [17, 32].

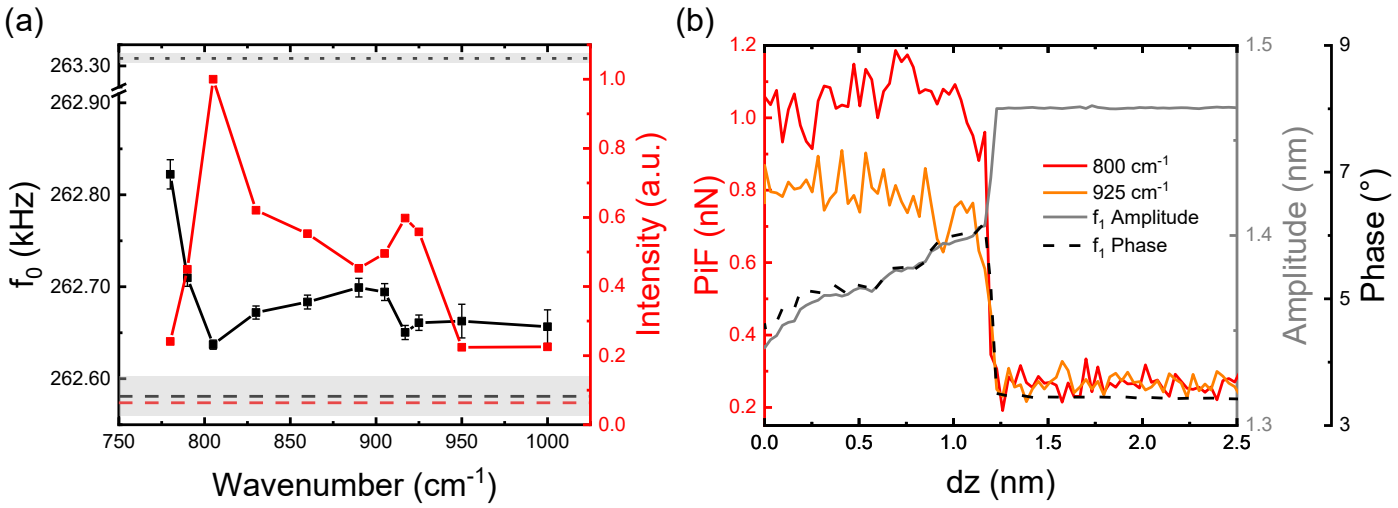

Figure 8: (a) Resonant frequency (black) and the intensities (red) of the first mechanical (PiF detection) mode of the cantilever (f_0), with certain incident laser wavenumbers on Sample 1. The dot lines mark the values when the tip is free oscillating away from the sample surface. The dash lines indicate the values when the tip is engaged and without laser excitation. The grey areas indicate the two standard deviations. (b) Retracting curves of photo-induced force with the incident laser of 800 cm^{-1}(red) and 925 cm^{-1}(orange) . The corresponding (925 cm^{-1} incident laser) tip oscillating amplitude and phase of the second mechanical mode (f_1, for AFM feedback) are plotted in grey solid and black dash line, individually.

Figure 8(b) shows the representative retracting curves at the two main PiF peaks, where $dz = 0$ corresponds to set-point tip position (cantilever oscillation amplitude about 2 *nm*) used to acquire PiF signals. Both curves show steep signal drop within 2 *nm* of the tip-sample height difference (dz). In the measurement at RRP, the simultaneously obtained AFM feedback amplitude and phase modulated at f_1 are also plotted. The amplitude shows a steep increase, indicating the tip detaching from the thin contamination (most likely water) layer on the sample surface even though the system was dry-air-purged (relative humidity RH < 20%). Compared to a free oscillating tip, AFM phase signal was known to shift upward when the tip working in the zone where attractive vdW force dominates [32]. Our measurement shows that the phase signal is higher before the tip retracted, again giving an evidence to the attractive non-contact PiF detection scheme.

These curves have high similarity with those observed by [37]. The sharp signal decrease suggests that the detected near-field dipole and thermal effects on SiC samples are efficiently mediated through the unavoidable spontaneous contamination in the tip-sample gap. Moreover, comparing the sideband PiF spectra of Sample 1 in figure 2(a,b), the relative peak intensities are reduced when using a brand new tip. We suppose that these features can play a role amplifying the local field. Conducting measurement in vacuum or more controlled humidity could be interesting in this regard. Furthermore, longer-range PiF decay are not substantially detected beyond the tip detachment point, strongly suggesting that a thermally induced photoacoustic effect is not involved here [37].

Critical Analysis of the Tip-Enhanced Absorption Model

While the simple tip-enhanced absorption model we propose reasonably replicates the observed signal consisting of two main peaks, some objections were raised in the discussion above. One mentioned concern is the need for a better account of the optical gap mode between the tip and the sample, which could better explain the great sensitivity of the RPP. Also, experimentally, we observe that the TO-related peak ~805 cm^{-1} provides minimal information about the local material properties, in stark contrast to the RPP peak, which is highly sensitive to local variations. We therefore question whether part of the RPP peak might originate from the illumination beam itself, rather than being entirely mediated by the tip, since this peak does not necessarily require a point tip for excitation. This would suggest the possibility to add terms to the model to incorporate contributions like induced dipole forces, which can also account for the peak at the RPP position, as it can also involve effective polarizability [36, 38].

Interestingly, the dips in f_0 observed in figure 8(a) seem to indicate a stronger attractive force near the TO peak and RPP compared to other wavelengths. These dips may again suggest an optically induced dipole-dipole force, typically regarded as attractive. However, a stronger modulation of van der Waals forces induced by photoabsorption may also explain this behavior, given that we are in the attractive AFM regime. Additionally, since the contamination layer plays a role, this interpretation may remain overly simplistic.

5. Application to SiC JFET characterization

In this study, we consider a semi-finished, unencapsulated P-type junction gate field-effect transistor (JFET) based on 4H-SiC. The fabrication process follows methods similar to those described in [66]. As illustrated in Figure 9(a), the layout consists of parallel P^+-doped (4×10^{19} cm^{-3}) source and drain fingers, along with N^+-doped ($4 \times 10^{19} cm^{-3}$) gate fingers, all patterned within a P-doped (10^{17} cm^{-3}) channel. The structures were fabricated using masked nitrogen and aluminum ion im-

plantation for N- and P-doping, respectively. However, due to lithographic constraints, the widths of the electrodes at the surface are wider than initially designed, as revealed by the scanning electron microscopy (SEM) image (Fig.9(b)), despite the correct functioning of the device. The observed contrast in the SEM image is primarily due to differences in conduction properties rather than topography, which remains relatively flat and shows little correlation with the contrast.

Based on previous measurements of homogeneous samples, a relatively low RPP intensity is expected in the N^+-doped region. Figure 9(d) presents a sideband PiF image taken at a laser wavelength near the RRP (915 cm^{-1}). This image aligns closely with the SEM image, distinguishing the different regions clearly. The unique characteristics of each zone are further supported by the PiFM spectral responses shown in Figure 9(c). As anticipated, the most intense RRP signal appears in the P-doped channel regions, which have lower doping levels. In contrast, the signal is weaker in the P^+-doped regions due to higher doping concentrations. In the N^+-doped regions, which contain more free electrons, the RRP signal is significantly dampened. In the overlapping P^+- and N^+-doped regions, the signal level falls between the levels observed in the isolated P^+ and N^+ regions.

Compared to free holes, electron mobility is significantly higher, and phonon-plasmon coupling is known to be stronger [64], leading to a more pronounced shift and damping in Raman spectra of N-doped SiC. As shown in the intensity traces in Figure 9(d), Raman mapping of the SiC LO phonon mode using a 325 nm laser on this JFET sample—although with lower spatial resolution and relatively weak contrast—reveals a trend consistent with the PiFM imaging results.

6. Conclusion

In summary, we have demonstrated the utility of the PiFM technique in assessing the surface quality of SiC samples at the nanoscale, particularly through the SPhP-related resonant mode. This mode significantly diminishes or disappears on implanted, doped or porous SiC samples. Similarly, the peak intensifies when an amorphous layer is annealed at a sufficient temperature, suggesting an efficient recrystallization process. PiFM images notably exhibit good lateral and depth resolution at the boundaries between thin SiC layers and the substrate. This data suggests that such a local probe technique could be particularly useful in monitoring the aging of SiC-based devices subjected to elevated temperatures or irradiation.

The obtained PiF spectrum was accounted for by considering the absorption power of the tip-enhanced evanescent field at the sample surface tip-sample junction. While the model based on the use of effective polarizability and loss term appears appealing due to its simplicity and analytical nature, additional phenomenological damping (beyond that provided by the far-field dielectric function) had to be added to account for the observed line broadening and resonant peak attenuation. Moreover, the presence of other non-negligible terms cannot be excluded based on the analysis of single materials like SiC. Further investigation using additional crystalline materials should lead to further refinements.

A closer examination of the tip resonant frequency suggested that the observed spectra reflect the influence of an attractive photo-induced effect, such as a modulation of vdW forces. The role of a thin contamination layer appears crucial in mediating the modulated force towards the tip, amplifying the detected signal. Finally, a first microelectronic device was mapped, showing promising sensitivity to doping concentration. The observed contrast appears much stronger and spatially resolved than what is obtained with micro-Raman, though the observed trends seem similar. Further hyper-spectral imaging on structured samples is anticipated to provide more valuable insights into local defects and lateral spatial resolution assessment, which is valuable in the context of microelectronic device characterization.

Acknowledgements

The authors thankfully acknowledge the financial support from the french National Research Agency, Temposcopy project, grant ANR-19-CE42-000,, as well as the support from the Nano-Phot graduate school in France.

Appendix A. Appendix

Appendix A.1. Finite dipole model

The finite dipole model considers the probe as an elongated conductive spheroid of total length $2L$, long enough to account for field enhancement but substantially shorter than the wavelength to remains reasonably in the quasi-static approximation. This model was successfully used to model s-SNOM experiments [23, 51], notably for better explaining the observed redshift of SPhP related resonance [52]. Despite the comprehensive derivation found in the literature, we briefly detail the expression we used in this work in order to be more explicit on the notation we use. The quantities involved are mostly presented in the Figure A.10 where a schematic comparison is made with the point dipole model.

In this model, it is typically assumed that the charges $\pm Q_0$ are induced by the illuminating field without the surface. They correspond to a first finite dipole of length $2L - 2W_0$. Once brought in interaction with the surface, the monopole $(-\beta Q_0)$ induced by the main interacting charge Q_0 creates a self field in the spheroid which is accounted by a second finite dipole. This second dipole is closer to the surface and consists in two charges $\pm Q_i$ separated by a shorter distance $L - W_i$, as depicted in the figure. With those notations, the effective polarizability expression can be expressed as:

$$\alpha_{eff}^{FD} = \alpha^{FD}\left(1 + \frac{f_0\beta}{1 - f\beta}\right),$$

$$f_0(\tilde{H}, \tilde{R}, g) = \left(g - 2\tilde{H} - \tilde{W}_0 - \tilde{R}\right)\frac{\ln(2\tilde{H} + \tilde{W}_0 + \tilde{R}/2)}{\ln(\tilde{R}/2)},$$

$$f(\tilde{H}, \tilde{R}, g) = \left(g - 2\tilde{H} - \tilde{W}_i - \tilde{R}\right)\frac{\ln(2\tilde{H} + \tilde{R})}{\ln(\tilde{R}/2)}$$

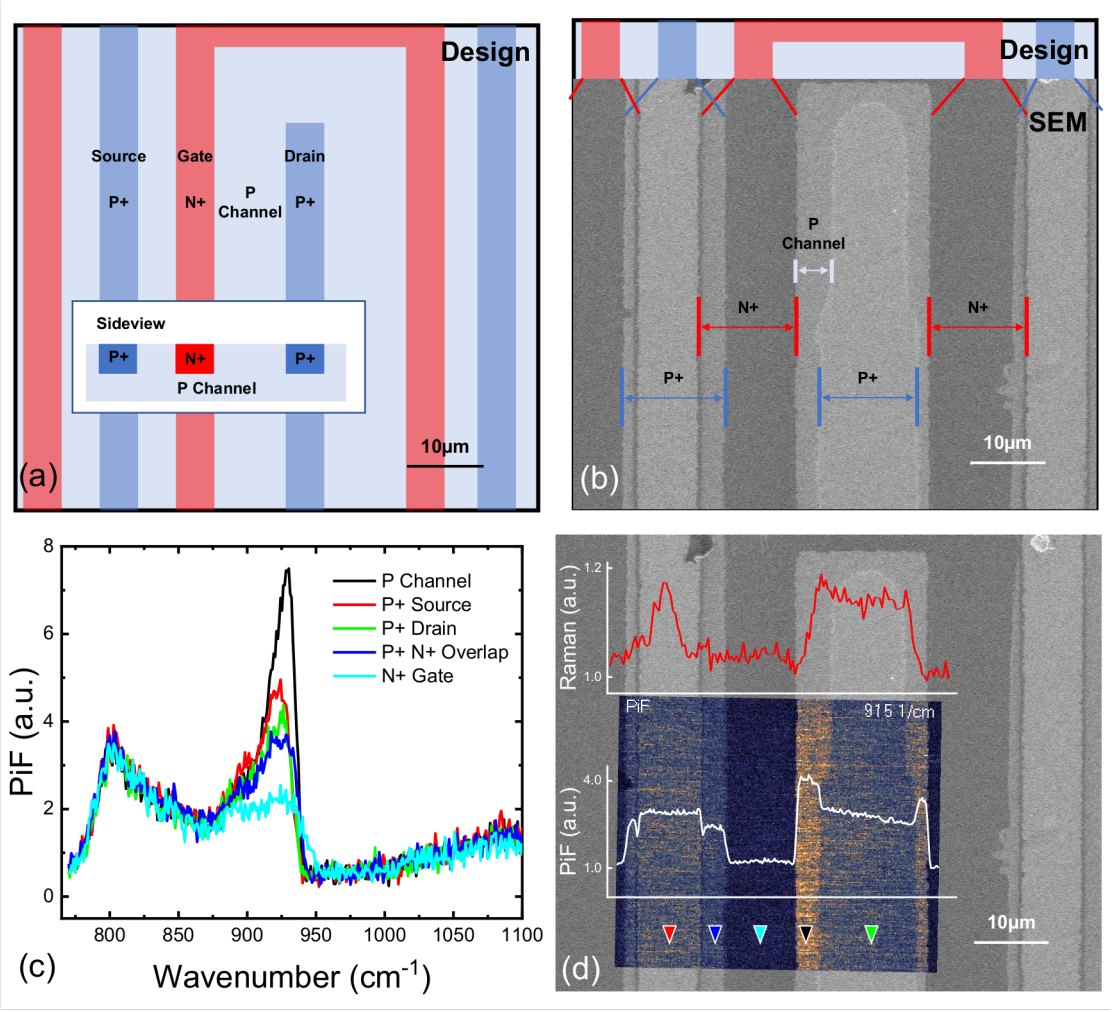

Figure 9: (a) Part of the layout design of a 4H-SiC based JFET sample. (b) SEM image of the fabrication result shows that the P^+ and N^+ doped regions are wider and overlapping in some places comparing to the original design. (c) Point PiF spectra taken in different regions on the sample (positions marked in (d)). (d) PiF image obtained near RRP (915 cm^{-1}), comparing to the SEM image. The inserts show the intensity traces of the Raman LO peak (968 cm^{-1}) and the PiF RRP.

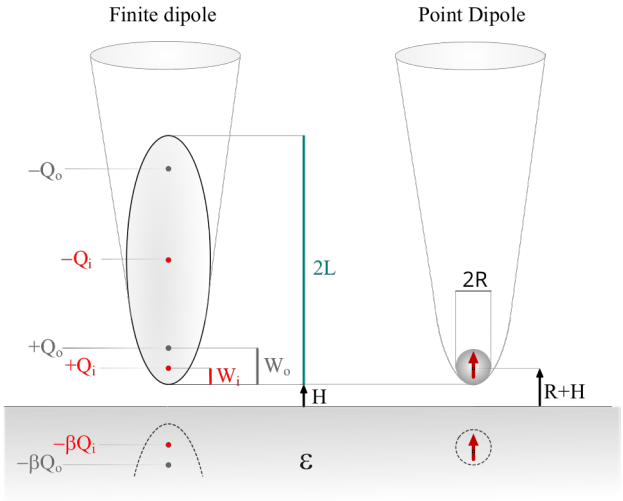

Figure A.10: Schematic comparison of the Finite Dipole Model and the Point Dipole model, providing the different scales involved. Far from a surface only the charges Q_0 and $-Q_0$ are present.The effective charges $\pm Q_i$ induced by the surface are mostly in the center and lower spheroid focus [51]

With $\alpha^{FD} = 2LQ_0/|E_i|$; $\tilde{H}$ and $\tilde{R}$ are the tip height and radius normalized to the effective tip length ($L \gg R$), that is, $\tilde{H} = \frac{H}{2L}$; $\tilde{R} = \frac{R}{2L}$. Following the mainly used estimations [51], $\tilde{W}_0 \approx \frac{1.31R}{2L+4R}$ is the normalized vertical position of Q_0 and $\tilde{W}_i \approx \frac{\tilde{R}}{4L}$ is the normalized position of Q_i. The factor g relates to the fraction of the involved charges in the tip. Previous studies [23, 52] show that the value remains mostly within (0.75 ± 0.05) for different spheroid shapes provided $2H + W_i > R/2$. In previous literature, s-SNOM data modeling with the FDM typically considers an additional complex exponential. The commonly reported value of $g = 0.7e^{0.06i}$ was also used in this work, as suggested in [23] and [51]. Finally, we note that in the expression of both f and f_0, g is large compared to the 3 others terms of the first factor. In other word, the correction we make on β in this paper to account for the RRP fluctuation can also approximately be seen as a modification of g when using the FDM.

Appendix A.2. Impact of scattering times values in the calculated spectra

It is observed that the intensity of the SPhP mode on SiC is very sensitive to the surface quality. In the Lorentz-Drude oscillator model, equation 1 in the main text, the spectral loss is dominated by the oscillator damping term (Γ) and the normalized carrier scattering time ($\tilde{\tau} = \tau \cdot \omega_p$) in the Drude's susceptibility (χ_{Drude}).

To clarify the contributions, we made parametric analysis on the SiC dielectric function (ϵ) and the Drude's susceptibility, based on the parameters retrieved from Sample 1 (Figure A.11(a,d)). As a reference, experimentally determined reststrahlen band (RB) of sample 1 is shown in magenta dash lines, with a black mark indicating the measured SPhP resonance peak. And the black dash curves trace the parameters giving the real permittivity $\epsilon' = -1$, that defines the SPhP resonance. With the increased Γ, the peak and valley of ϵ' shifts slightly away from the TO phonon frequency with reducing contrast, leading to a slight red-shift of the SPhP mode. Meanwhile, the imaginary part (ϵ'') expands and become larger in the original RB range, implying more loss in the spectrum. Figure A.11(b,c) plots the corresponding calculated quasi-static reflection coefficient (β) and the total absorption (P). On the other hand, increasing the normalized carrier scattering time ($\tilde{\tau}$) blue shifts the SPhP resonance while the spectral loss crosses through a maximal and returns, resulting in a minor effect on the intensity of the SPhP mode, as plotted in Figure A.11(e,f).

References

[1] T. Kimoto, Material science and device physics in SiC technology for high-voltage power devices, Japanese Journal of Applied Physics 54 (4) (2015) 040103. doi:10.7567/jjap.54.040103.

[2] S. Ji, Z. Zhang, F. Wang, Overview of high voltage sic power semiconductor devices: development and application, CES Transactions on Electrical Machines and Systems 1 (3) (2017) 254–264. doi:10.23919/tems.2017.8086104.

[3] M. Li, X. Zhou, H. Yang, S. Du, Q. Huang, The critical issues of SiC materials for future nuclear systems, Scripta Materialia 143 (2018) 149–153. doi:10.1016/j.scriptamat.2017.03.001.

[4] Y. Katoh, L. L. Snead, I. Szlufarska, W. J. Weber, Radiation effects in SiC for nuclear structural applications, Current Opinion in Solid State and Materials Science 16 (3) (2012) 143–152. doi:10.1016/j.cossms.2012.03.005.

[5] A. Lohrmann, B. C. Johnson, J. C. McCallum, S. Castelletto, A review on single photon sources in silicon carbide, Reports on Progress in Physics 80 (3) (2017) 034502. doi:10.1088/1361-6633/aa5171.

[6] S. Castelletto, A. Boretti, Silicon carbide color centers for quantum applications, Journal of Physics: Photonics 2 (2) (2020) 022001. doi:10.1088/2515-7647/ab77a2.

[7] R. Wu, K. Zhou, C. Y. Yue, J. Wei, Y. Pan, Recent progress in synthesis, properties and potential applications of SiC nanomaterials, Progress in Materials Science 72 (2015) 1–60. doi:10.1016/j.pmatsci.2015.01.003.

[8] M. Huff, Review paper: Residual stresses in deposited thin-film material layers for micro- and nano-systems manufacturing, Micromachines 13 (12) (2022) 2084. doi:10.3390/mi13122084.

[9] S. Saddow, Silicon carbide technology for advanced human healthcare applications, Micromachines 13 (3) (2022) 346. doi:10.3390/mi13030346.

[10] J. S. Ponraj, S. C. Dhanabalan, G. Attolini, G. Salviati, SiC nanostructures toward biomedical applications and its future challenges, Critical Reviews in Solid State and Materials Sciences 41 (5) (2016) 430–446. doi:10.1080/10408436.2016.1150806.

[11] H. Harima, Raman scattering characterization on SiC, Microelectronic Engineering 83 (1) (2006) 126–129. doi:10.1016/j.mee.2005.10.037.

[12] M. Zhang, J. Huang, R. Hong, X. Chen, Z. Wu, Annealing effects on structural, optical and electrical properties of al implanted 4h-SiC, in: 2009 IEEE International Conference of Electron Devices and Solid-State Circuits (EDSSC), IEEE, 2009, pp. 314–317. doi:10.1109/edssc.2009.5394252.

[13] S. Amarie, F. Keilmann, Broadband-infrared assessment of phonon resonance in scattering-type near-field microscopy, Physical Review B 83 (4) (jan 2011). doi:10.1103/physrevb.83.045404.

[14] X. Chen, D. Hu, R. Mescall, G. You, D. Basov, Q. Dai, M. Liu, Modern scattering-type scanning near-field optical microscopy for advanced material research, Advanced Materials 31 (24) (2019) 1804774.

[15] J. J. Schwartz, D. S. Jakob, A. Centrone, A guide to nanoscale ir spectroscopy: resonance enhanced transduction in contact and tapping mode afm-ir, Chemical Society Reviews 51 (13) (2022) 5248–5267.

[16] J. Mathurin, A. Deniset-Besseau, D. Bazin, E. Dartois, M. Wagner, A. Dazzi, Photothermal afm-ir spectroscopy and imaging: Status, challenges, and trends, Journal of Applied Physics 131 (1) (2022).

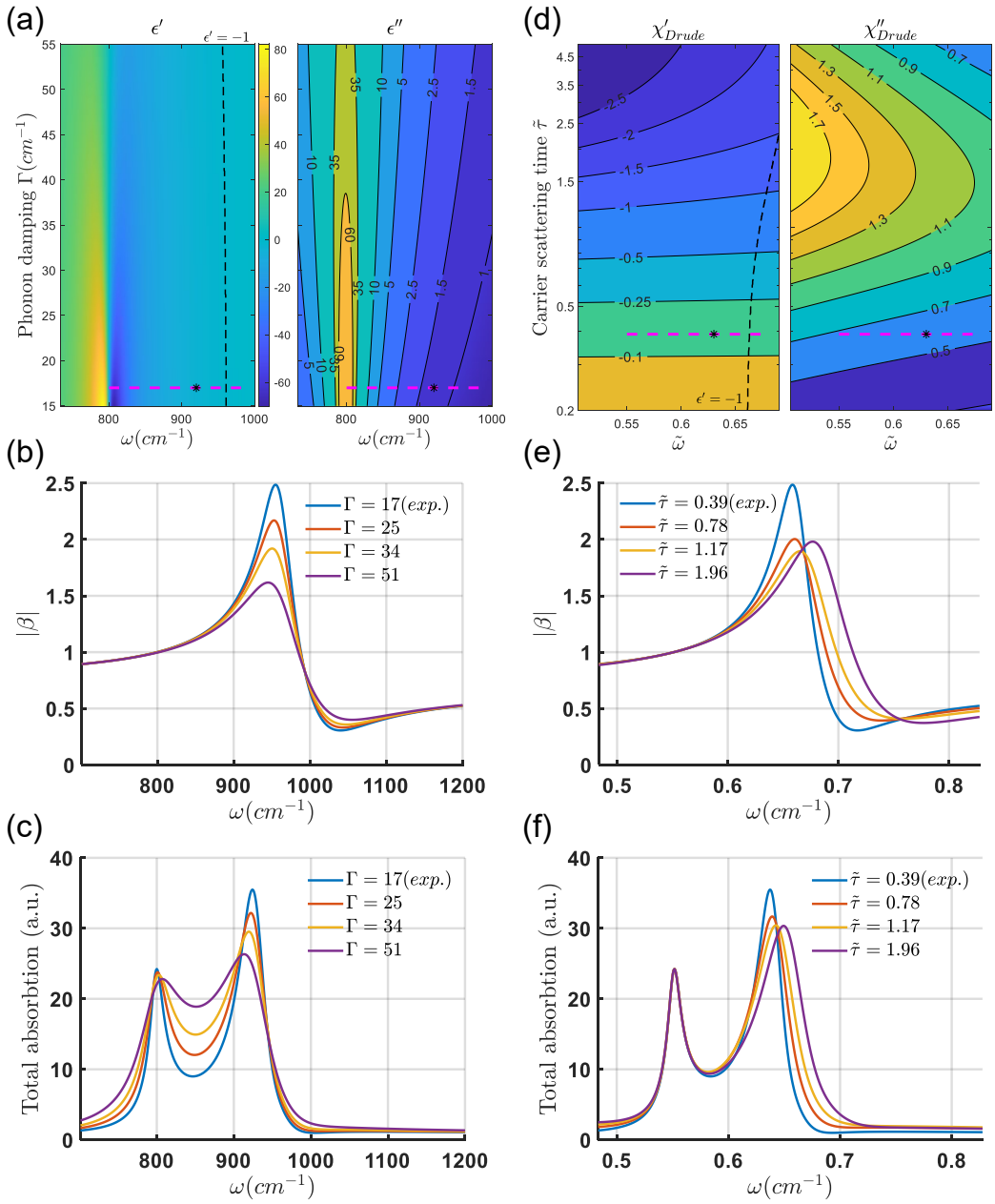

Figure A.11: Parametric map of (a)SiC permittivity (ϵ) as a function of Γ and ω; (d)Drude's susceptibility (χ_{Drude}) as a function of normalized $\tilde{\tau}$ and $\tilde{\omega}$. The magenta dash lines show the RB determined on Sample 1, with a black mark indicating the measured SPhP resonance peak. Black dash curves indicate where $\epsilon' = -1$. (b,e) plot the corresponding $|\beta|$. (c,f) plot the simulated total absorption results.

[17] A. A. Sifat, J. Jahng, E. O. Potma, Photo-induced force microscopy (pifm)–principles and implementations, Chemical Society Reviews 51 (11) (2022) 4208–4222.

[18] J. A. Davies-Jones, P. R. Davies, Photo induced force microscopy: chemical spectroscopy beyond the diffraction limit, Materials Chemistry Frontiers 6 (12) (2022) 1552–1573.

[19] R. Hillenbrand, T. Taubner, F. Keilmann, Phonon-enhanced light–matter interaction at the nanometre scale, Nature 418 (6894) (2002) 159–162.

[20] B. Hauer, C. E. Marvinney, M. Lewin, N. A. Mahadik, J. K. Hite, N. Bassim, A. J. Giles, R. E. Stahlbush, J. D. Caldwell, T. Taubner, Exploiting phonon-resonant near-field interaction for the nanoscale investigation of extended defects, Advanced Functional Materials 30 (10) (jan 2020). doi:10.1002/adfm.201907357.

[21] A. J. Huber, A. Ziegler, T. Köck, R. Hillenbrand, Infrared nanoscopy of strained semiconductors, Nature Nanotechnology 4 (3) (2009) 153–157. doi:10.1038/nnano.2008.399.

[22] A. M. Gigler, A. J. Huber, M. Bauer, A. Ziegler, R. Hillenbrand, R. W. Stark, Nanoscale residual stress-field mapping around nanoindents in SiC by IR s-SNOM and confocal raman microscopy, Optics Express 17 (25) (2009) 22351. doi:10.1364/oe.17.022351.

[23] A. Cvitkovic, N. Ocelic, R. Hillenbrand, Analytical model for quantitative prediction of material contrasts in scattering-type near-field optical microscopy, Optics Express 15 (14) (2007) 8550. doi:10.1364/oe.15.008550.

[24] A. Huber, N. Ocelic, T. Taubner, R. Hillenbrand, Nanoscale resolved infrared probing of crystal structure and of plasmon-phonon coupling, Nano Letters 6 (4) (2006) 774–778. doi:10.1021/nl060092b.

[25] L. Mester, A. A. Govyadinov, R. Hillenbrand, High-fidelity nano-ftir spectroscopy by on-pixel normalization of signal harmonics, Nanophotonics 11 (2) (2021) 377–390.

[26] J. Jahng, B. Kim, E. S. Lee, E. O. Potma, Quantitative analysis of sideband coupling in photoinduced force microscopy, Physical Review B 94 (19) (nov 2016). doi:10.1103/physrevb.94.195407.

[27] Q. Xie, X. G. Xu, What do different modes of afm-ir mean for measuring soft matter surfaces?, Langmuir 39 (49) (2023) 17593–17599.

[28] R. A. Murdick, W. Morrison, D. Nowak, T. R. Albrecht, J. Jahng, S. Park, Photoinduced force microscopy: A technique for hyperspectral nanochemical mapping, Japanese Journal of Applied Physics 56 (8S1) (2017) 08LA04. doi:10.7567/jjap.56.08la04.

[29] D. Nowak, W. Morrison, H. K. Wickramasinghe, J. Jahng, E. Potma, L. Wan, R. Ruiz, T. R. Albrecht, K. Schmidt, J. Frommer, D. P. Sanders, S. Park, Nanoscale chemical imaging by photoinduced force microscopy, Science Advances 2 (3) (mar 2016). doi:10.1126/sciadv.1501571.

[30] J. Jahng, E. O. Potma, E. S. Lee, Tip-enhanced thermal expansion force for nanoscale chemical imaging and spectroscopy in photoinduced force microscopy, Analytical Chemistry 90 (18) (2018) 11054–11061. doi:10.1021/acs.analchem.8b02871.

[31] M. A. Almajhadi, S. M. A. Uddin, H. K. Wickramasinghe, Observation of nanoscale opto-mechanical molecular damping as the origin of spectroscopic contrast in photo induced force microscopy, Nature communications 11 (1) (2020) 5691. doi:10.1038/s41467-020-19067-3.

[32] M. Giocondo, E. Bruno, E. Lacaze, L. De Stefano, M. P. De Santo, P. Giardina, S. Houmadi, S. Longobardi, Atomic force spectroscopies: A toolbox for probing the biological matter, in: C. Frewin (Ed.), Atomic Force Microscopy Investigations Into Biology: From Cell to Protein, BoD–Books on Demand, 2012, Ch. 1, pp. 3–28.

[33] A. Ambrosio, M. Tamagnone, K. Chaudhary, L. A. Jauregui, P. Kim, W. L. Wilson, F. Capasso, Selective excitation and imaging of ultraslow phonon polaritons in thin hexagonal boron nitride crystals, Light: Science & Applications 7 (1) (2018) 27. doi:10.1038/s41377-018-0039-4.

[34] C. Luo, X. Guo, H. Hu, D. Hu, C. Wu, X. Yang, Q. Dai, Probing polaritons in 2D materials, Advanced Optical Materials 8 (5) (2020) 1901416. doi:10.1002/adom.201901416.

[35] M. Almajhadi, H. K. Wickramasinghe, Contrast and imaging performance in photo induced force microscopy, Optics Express 25 (22) (2017) 26923. doi:10.1364/oe.25.026923.

[36] Y. Huang, D. Legrand, R. Vincent, E. A. D. Foli, D. Nowak, G. Lerondel, R. Bachelot, T. Taliercio, F. Barho, L. Cerutti, F. Gonzalez-Posada, B. K. Tay, A. Bruyant, Spectroscopic nanoimaging of all-semiconductor plasmonic gratings using photoinduced force and scattering type nanoscopy, ACS Photonics 5 (11) (2018) 4352–4359. doi:10.1021/acsphotonics.8b00700.

[37] B. T. O'Callahan, J. Yan, F. Menges, E. A. Muller, M. B. Raschke, Photoinduced tip–sample forces for chemical nanoimaging and spectroscopy, Nano Letters 18 (9) (2018) 5499–5505. doi:10.1021/acs.nanolett.8b01899.

[38] J. Li, J. Jahng, X. Ma, J. Liang, X. Zhang, Q. Min, X.-L. Wang, S. Chen, E. S. Lee, X.-H. Xia, Surface-phonon-polariton-enhanced photoinduced dipole force for nanoscale infrared imaging, National Science Review 11 (5) (2024) nwae101.

[39] B. Ji, A. Kenaan, S. Gao, J. Cheng, D. Cui, H. Yang, J. Wang, J. Song, Label-free detection of biotoxins via a photo-induced force infrared spectrum at the single-molecular level, Analyst 144 (20) (2019) 6108–6117.

[40] J. Jahng, E. O. Potma, E. S. Lee, Nanoscale spectroscopic origins of photoinduced tip–sample force in the midinfrared, Proceedings of the National Academy of Sciences 116 (52) (2019) 26359–26366.

[41] Y. Zhao, Z. Yao, C. D. Snow, Y. Xu, Y. Wang, D. Xiu, L. A. Belfiore, J. Tang, Stable fluorescence of eu3+ complex nanostructures beneath a protein skin for potential biometric recognition, Nanomaterials 11 (9) (2021) 2462. doi:10.3390/nano11092462.

[42] B. Kim, J. Jahng, A. Sifat, E. S. Lee, E. O. Potma, Monitoring fast thermal dynamics at the nanoscale through frequency domain photoinduced force microscopy, The Journal of Physical Chemistry C 125 (13) (2021) 7276–7286.

[43] A. C. Tam, Applications of photoacoustic sensing techniques, Reviews of Modern Physics 58 (2) (1986) 381. doi:10.1103/RevModPhys.58.381.

[44] G. E. Sommargren, Optical heterodyne profilometry, Applied Optics 20 (4) (1981) 610–618.

[45] M. T. Cuberes, H. Assender, G. A. D. Briggs, O. Kolosov, Heterodyne force microscopy of pmma/rubber nanocomposites: nanomapping of viscoelastic response at ultrasonic frequencies, Journal of Physics D: Applied Physics 33 (19) (2000) 2347. doi:10.1088/0022-3727/33/19/301.

[46] G. Gautier, J. Biscarrat, D. Valente, T. Defforge, A. Gary, F. Cayrel, Systematic study of anodic etching of highly doped n-type 4h-sic in various hf based electrolytes, Journal of The Electrochemical Society 160 (9) (2013) D372. doi:10.1149/2.082309jes.

[47] E. Usureau, E. Vuillermet, M. Lazar, A. Andrieux, A. Jacquemot, High quality single crystal recrystallization of thin 4h-sic films deposed by pvd techniques, a way for new emerging fields, Solid State Phenomena 343 (2023) 21–28.

[48] M. Lazar, S. Sejil, L. Lalouat, C. Raynaud, D. Carole, D. Planson, G. Ferro, F. Laariedh, C. Brylinski, H. Morel, p-type doping of 4h-sic for integrated bipolar and unipolar devices, Romanian Journal of Information Science and Technology 18 (4) (2015) 329–342.

[49] J. Chahal, N. Rahbany, Y. El-Helou, K. Wu, A. Bruyant, C. Zgheib, M. Kazan, Temperature dependence of the anisotropy of the infrared dielectric properties and phonon-plasmon coupling in n-doped 4h-sic, Journal of Physics and Chemistry of Solids 187 (2024) 111861. doi:10.1016/j.jpcs.2023.111861.

[50] F. Keilmann, R. Hillenbrand, Near-field microscopy by elastic light scattering from a tip, Philosophical Transactions of the Royal Society of London. Series A: Mathematical, Physical and Engineering Sciences 362 (1817) (2004) 787–805. doi:10.1098/rsta.2003.1347.

[51] A. A. Govyadinov, I. Amenabar, F. Huth, P. S. Carney, R. Hillenbrand, Quantitative measurement of local infrared absorption and dielectric function with tip-enhanced near-field microscopy, The journal of physical chemistry letters 4 (9) (2013) 1526–1531.

[52] A. Jarzembski, K. Park, Finite dipole model for extreme near-field thermal radiation between a tip and planar sic substrate, Journal of Quantitative Spectroscopy and Radiative Transfer 191 (2017) 67–74.

[53] D. B. Mawhinney, J. A. Glass, J. T. Yates, Ftir study of the oxidation of porous silicon, The Journal of Physical Chemistry B 101 (7) (1997) 1202–1206.

[54] N. Delpuech, D. Mazouzi, N. Dupre, P. Moreau, M. Cerbelaud, J. Bridel, J.-C. Badot, E. De Vito, D. Guyomard, B. Lestriez, et al., Critical role of silicon nanoparticles surface on lithium cell electrochemical performance analyzed by ftir, raman, eels, xps, nmr, and bds spectroscopies, The Journal of Physical Chemistry C 118 (31) (2014) 17318–17331.

[55] E. Riedo, F. Lévy, H. Brune, Kinetics of capillary condensation in nanoscopic sliding friction, Physical review letters 88 (18) (2002)

185505.

[56] S. Gómez-Monivas, J. J. Sáenz, M. Calleja, R. García, Field-induced formation of nanometer-sized water bridges, Physical review letters 91 (5) (2003) 056101.

[57] Z. C. Feng, A. Rohatgi, C. C. Tin, R. Hu, A. T. S. Wee, K. P. Se, Structural, optical, and surface science studies of 4h-SiC epilayers grown by low pressure chemical vapor deposition, Journal of Electronic Materials 25 (5) (1996) 917–923. doi:10.1007/bf02666658.

[58] S. Patabendigedara, D. Nowak, M. J. Nancarrow, S. M. Clark, Determining the water content of nominally anhydrous minerals at the nanometre scale, Review of Scientific Instruments 92 (2) (2021). doi:10.1063/5.0025570.

[59] K.-T. Wu, E. Vuillermet, E. Usureau, Y. El-Helou, M. Kazan, W.-Y. Woon, M. Lazar, A. Bruyant, Sic structural characterization by non destructive near-field microscopy techniques, in: 2022 International Semiconductor Conference (CAS), 2022, pp. 73–76. doi:10.1109/CAS56377.2022.9934358.

[60] A. Dazzi, F. Glotin, R. Carminati, Theory of infrared nanospectroscopy by photothermal induced resonance, Journal of Applied Physics 107 (12) (2010).

[61] L. Novotny, B. Hecht, Principles of nano-optics, Cambridge University, 2012, chap. 14, pp. 446-472.

[62] B. T. O'Callahan, W. E. Lewis, A. C. Jones, M. B. Raschke, Spectral frustration and spatial coherence in thermal near-field spectroscopy, Physical Review B 89 (24) (2014) 245446. doi:10.1103/PhysRevB.89.245446.

[63] M. Shamseddine, M. Kazan, M. Tabbal, Model for the unpolarized infrared reflectivity from uniaxial polar materials: Effects of anisotropy, free carriers, and defects, Infrared Physics & Technology 55 (1) (2012) 112–121.

[64] H. Harima, S.-i. Nakashima, T. Uemura, Raman scattering from anisotropic lo-phonon–plasmon–coupled mode in n-type 4h–and 6h–sic, Journal of applied physics 78 (3) (1995) 1996–2005.

[65] Z. Fei, G. O. Andreev, W. Bao, L. M. Zhang, A. S. McLeod, C. Wang, M. K. Stewart, Z. Zhao, G. Dominguez, M. Thiemens, et al., Infrared nanoscopy of dirac plasmons at the graphene–sio2 interface, Nano letters 11 (11) (2011) 4701–4705.

[66] M. Lazar, F. Laariedh, P. Cremillieu, D. Planson, J.-L. Leclercq, The channeling effect of al and n ion implantation in 4h–sic during jfet integrated device processing, Nuclear Instruments and Methods in Physics Research Section B: Beam Interactions with Materials and Atoms 365 (2015) 256–259.